Fluorous Liquids for Magnetic Resonance-based Thermometry with Enhanced Responsiveness and Environmental Degradation

Jiaqian Li,[†] Thomas F. Mundhenke,[‡] Thomas G. Smith, [†] William A. Arnold,[‡] William C.K. Pomerantz[*,†]

[†] Department of Chemistry, University of Minnesota, 207 Pleasant Street SE, Minneapolis, Minnesota 55455, United States

[‡] Department of Civil, Environmental, and Geo-Engineering, University of Minnesota, 500 Pillsbury Dr. SE, Minneapolis, Minnesota 55455, United States

ABSTRACT: Accurate temperature measurement via magnetic resonance is valuable for both *in vitro* and *in vivo* analysis of local tissue for evaluating disease pathology and medical interventions. ^{1}H MRI-based thermometry is used clinically, but is susceptible to error from magnetic field drift, low sensitivity in fatty tissue, and requires a reference for absolute temperature determination. As an alternative, perfluorotributylamine (PFTBA), a perfluorocarbon liquid for ^{19}F MRI thermometry, is based on chemical shift responsiveness and approaches the sensitivity of ^{1}H MRI thermometry agents; however, environmental persistence, greenhouse gas concerns, and multiple resonances which can lead to MRI artifacts indicate a need for alternative sensors. Using a ^{19}F NMR-based structure-property study of synthetic organofluorine molecules, this research develops new organofluorine liquids with improved temperature responsiveness, high signal, and reduced non-magnetically equivalent fluorine resonances. Environmental degradation analysis using reverse-phase HPLC and quantitative ^{19}F NMR demonstrates a rapid degradation profile mediated via the arylfluorine core of the temperature sensors. Our findings show our lead liquid temperature sensor, **DD-1**, can be made in high yield in a single step and possesses an improved responsiveness over our prior work and an 83% increase in aqueous thermal responsiveness over PFTBA. Degradation studies indicate robust degradation with half-lives of less than two hours under photolysis conditions for the parent compound and formation of other fluorinated products. The improved performance of **DD-1** and susceptibility to environmental degradation highlights a new lead fluorous liquid for thermometry applications.

Non-invasive measurement of temperature is vital for determining local tissue temperatures. These measurements are used for evaluating disease pathology and medical interventions such as high intensity focused ultrasound,[1] low temperature hyperthermia,[2] hypothermia,[3] radiofrequency ablation,[4] and thermal ablation.[5] Additionally, *in vivo* oximetry measurements are also sensitive to temperature fluctuations, requiring accurate temperature determination.[6] Magnetic resonance imaging (MRI) is one such approach that is used in the clinic. The gold standard thermometry measurement is based on changes in the proton-resonance frequency of water (PRF) with the highest responsiveness in most tissues of ~10×10^{-3} ppm/°C.[7] However, for absolute temperature measurements, reference frequencies are required. PRF temperature measurements are also susceptible to error from magnetic field drift and have low sensitivity in fatty tissue.[1] Such limitations have led to the development of heteronuclear approaches including using ^{23}Na,[8] ^{129}Xe,[9] and ^{19}F.

Fluorine-based magnetic resonance applications have been mainly limited to preclinical studies due to current limitations in the availability of ^{19}F MRI systems for clinical use. There are several advantages of ^{19}F-magnetic resonance that make this an attractive strategy for further development. Given its similar gyromagnetic ratio to ^{1}H, ^{19}F is the second most sensitive stable NMR active nucleus, with 83% signal sensitivity relative to ^{1}H. In addition, the absence of naturally occurring mobile fluorine provides a background-free spectrum that can be used in combination with ^{1}H MRI for anatomical imaging.[10] Organofluorine temperature sensors have previously been developed based on changes in nuclear relaxation or chemical shift changes.[11,12] Perfluorocarbon liquids are particularly attractive for formulating into nanoemulsions or encapsulating into nanoparticles. These fluorous liquid formulations help overcome the inherently low sensitivity of magnetic resonance measurements for *in vivo* cell tracking studies, oximetry, and thermometry.[10,13–15]

The perfluorocarbon liquid, perfluorotributylamine (PFTBA, **Figure 1**), was the first organofluorine compound to be used for *in vivo* thermometry with a temperature responsiveness of ~9×10^{-3} ppm/°C approaching the PRF responsiveness and remains one of the most responsive ^{19}F sensors.[16] Given the temperature dependence of fluorocarbon-based oximetry agents, based on T_1 relaxation,[17] PFTBA can be used in combination for temperature calibration. However, several potential difficulties are encountered when using PFTBA including multiple resonances with similar frequencies. These resonances may lead to chemical shift artifacts and a responsiveness below the PRF.[18] Additionally, PFTBA is a potent greenhouse gas.[19] There is also heightened concern about use and environmental persistence of compounds with perfluorinated alkyl groups.[19–21]

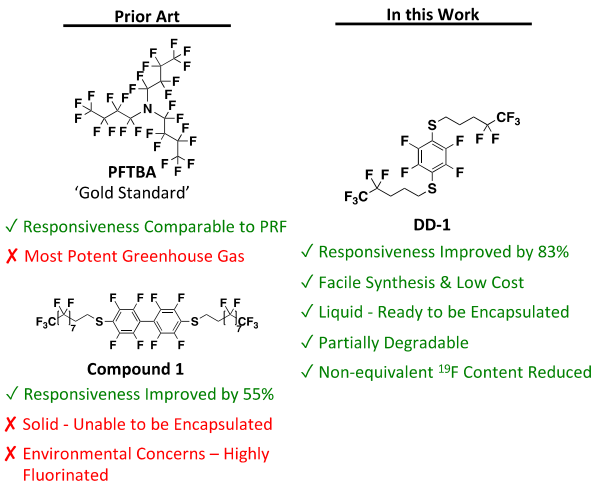

Figure 1. Molecular structures and attributes of current and previously reported fluorinated magnetic resonance-based thermometry agents PFTBA, **1** and **DD-1**.

Previously we reported new organofluorine temperature sensors including **1** (**Figure 1**) through a combined experimental and computational approach that improved upon the PFTBA temperature responsiveness and PRF by almost two-fold.[22] However, **1** possessed several key limitations. The first was a concern over too many fluorine resonances of similar chemical shift which could lead to chemical shift artifacts for ^{19}F MRI. The second concern was that similar to PFTBA, **1** still possessed a long polyfluorinated tail, raising concerns over environmental persistence. Finally, while PFTBA is a room temperature liquid and is readily formulated in our mesoporous silica nanoparticles, **1** is a solid making this process significantly more challenging.[22,23] To address these challenges, we sought to redesign our original temperature sensors, using shorter fluorinated tails based on prior computational predictions, [22] while evaluating heteroatom effects, and the aromatic core on phase behavior and temperature responsiveness. We further evaluated the potential for degradation under simulated environmental and wastewater treatment conditions for three of our lead candidates. We conclude from these studies, that short fluorine chains attached to a perfluoroaromatic core provide simplified and more responsive temperature sensors than PFTBA and our previous sensors, and a liquid phase for future loading studies into nanoparticles. Degradation analyses further show that incorporation of arylfluorine groups lead to more readily degraded parent compounds than perfluoroalkyl substances [24] and should be beneficial for designing future organofluorine materials beyond temperature sensors.

EXPERIMENTAL

^{19}F NMR Variable Temperature Measurements. For temperature measurements in organic solvent, compounds were dissolved in THF-d_8 and measured with Bruker AVANCE III 500 equipped with a 5 mm BBFO SmartProbe. For measure of compounds dissolved in THF-d_8, ^{19}F spectra were obtained at 471 MHz with dummy scans = 4, acquisition time = 0.57 s, delay time = 1 s, pre-scan delay = 6.5 µs, and the number of scans = 16. The temperature was increased by passing heated N_2 gas over the spinning sample which was monitored by an internal instrument temperature probe. The temperature was allowed to stabilize for 3 min before scanning. For temperature measurements in aqueous solution, compounds were dissolved in DMSO first and then added to 10 mM pH = 6.9 phosphate buffer/D_2O (9:1 v/v) to make 5% DMSO stock in 500 µL phosphate buffer/D_2O. Samples were measured with Bruker AVANCE III 500 equipped with a 5 mm BBFO SmartProbe. ^{19}F spectra were obtained at 471 MHz with dummy scans = 4, acquisition time = 0.57 s, delay time = 1 s, pre-scan delay = 6.5 µs, and the number of scans = 2048. The temperature was increased by passing heated N_2 gas over the spinning sample which was monitored by an internal instrument temperature probe. The temperature was allowed to stabilize for 10 min before scanning.

^{19}F NMR Aqueous Solubility Limit Measurements. Compound was dissolved in DMSO and then added to 10 mM pH = 6.9 phosphate buffer/D_2O (9:1 v/v) to make 5% DMSO stock in 500 µL phosphate buffer/D_2O at concentration of 10/50/100/150/200/250 µM. Samples were measured with Bruker AVANCE III 500 equipped with a 5 mm BBFO SmartProbe. ^{19}F spectra were obtained at 471 MHz with dummy scans = 4, acquisition time = 0.57 s, delay time = 1 s, pre-scan delay = 6.5 µs, and the number of scans = 800.

UV-Visible Spectra. Stock solutions of **DD-1**, **DD-3**, and **DD-5** were prepared at 10 mM in DMSO and stored in the dark. A 10 mM phosphate buffer at pH 7 was prepared and stock solutions were diluted to 50 µM. UV-visible absorption spectra were obtained using a Horiba Aqualog.

Photolysis Experiments. Stock solutions were diluted to 10 µM in the phosphate buffer for kinetic experiments and 50 µM for ^{19}F NMR experiments. Solutions were placed in 10 mL quartz tubes sealed with cork stoppers with no contact to the solution. The solutions were photolyzed in (i) an Atlas Suntest CPS+ solar simulator with a 1500 W xenon lamp at an intensity of 765 W m^{-2} using a wavelength range of 290-800 nm at a 30° angle, and (ii) a 450 W medium pressure polychromatic mercury vapor lamp with a quartz immersion well with cooling water circulation, a Pyrex 280 nm cutoff filter (Ace Glass), and a merry-go-round sample holder. Samples were photolyzed until ~60 to 80% degradation of the parent compound was achieved. For each compound an equivalent tube was prepared and wrapped in aluminum foil as a dark control. Experiments were performed in triplicate.

Photolysis Kinetics and Quantum Yields. A minimum of five spaced time points ranging from 60-180 min for the solar simulator and 20-60 min for the mercury vapor lamp were taken to determine the loss of the parent compound concentration using high-pressure liquid chromatography (HPLC) combined with a variable wavelength UV detector (Agilent 1100 series). First order rate constants were found by regression of $\ln(C/C_0)$ versus time where C_0 is the initial concentration and C is the concentration in µM. The direct photolysis quantum yields in the solar simulator were found using a p-nitroanisole-pyridine (PNA-PYR) actinometer and relationships from Dulin and Mill,[25] Leifer[26] and updated calculations by Laszakovits et al. [27]

Ozone-mediated degradation. The 10 mM DMSO stock solution of **DD-1** was used to make 100 mL of a 50 µM solution in the 10 mM pH = 7 phosphate buffer. The solution was placed in an Erlenmeyer flask in an ice bath. Ozone (O_3) was produced using ultra-high pure oxygen gas (99.99%) with a Pacific Ozone O_3 generator and bubbled directly into the sample solution. O_3 concentration was previously measured using

UV-Vis spectroscopy (Beckman Coulter DU 530). The concentration of O_3 (with an ε =3000 M^{-1} cm^{-1}) was determined by direct absorbance at 258 nm. By using a 3:1 dilution, the absorbance obtained is equivalent to the O_3 concentration in mM.[28] After 30 minutes the O_3 concentration in ultrapure water was 0.61 mM or 29.16 mg/L. Samples were taken over time for 300 minutes and parent compound degradation was monitored via HPLC. O_3 was chosen to simulate oxidation processes used in water and wastewater treatment plants.[29,30] O_3 is a selective oxidant that rapidly degrades in aqueous environments to an array of reactive oxygen species, including hydroxyl radical (•OH) which a non-selective oxidant.[29]

RESULTS AND DISCUSSION

Design and Synthesis of Second-Generation Fluorinated Temperature Sensors. To improve upon the phase behavior and thermal responsiveness of **1**, we designed several second generation fluorinated small molecules through variation in the aromatic core, fluorinated tail length, and heteroatom oxidation state (**DD-1**–**DD-7**, **Figure 2**). All temperature sensors maintained the structural symmetry for increasing the number of magnetically equivalent fluorine atoms for high signal sensitivity. With the exception of **DD-7**, these sensors also reduce the overall number of fluorine resonances which could lead to potential artifacts in ^{19}F magnetic resonance applications. The selection of aromatic cores in our temperature sensor design was also expanded. While **1** had a perfluorobiphenyl core, a similarly responsive analog **2** had a more simplified perfluorophenyl core. Inclusion of these aryl fluorine groups were important as the respective ^{19}F resonances were

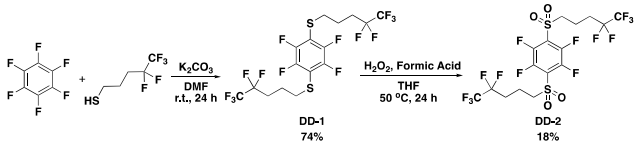

Name	Aromatic Core	Aliphatic Chain R=	State	Yield %
DD-1		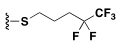	Liquid	74
DD-2		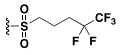	Solid	18
2		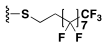	Solid	18
DD-3		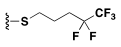	Liquid	62
DD-4	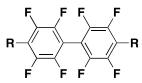	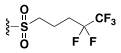	Solid	35
1		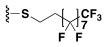	Solid	33
DD-5	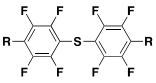	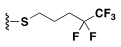	Solid	78
DD-6	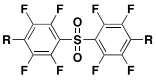	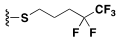	Solid	53
DD-7		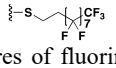	Solid	20

Figure 2. Synthesis, structures of fluorinated temperature sensors, and corresponding room temperature phase behavior. Top) Representative synthetic scheme of **DD-1** and **DD-2**. Bottom) Structure of **DD-1**–**DD-7** and compound **1** and **2** with corresponding phase characteristics.

essential for maintaining a high temperature responsiveness. In addition, a structurally similar perfluorophenyl sulfide and a perfluorophenyl sulfone core were introduced to evaluate if these functional groups would lead to additional thermal responsiveness or alter the phase behavior of the final compound through introduction of two additional rotatable bonds. Secondly, based on our previous computational predictions, a shorter alkyl chain containing a perfluoroethyl group was predicted to slightly improve the thermal responsiveness while reducing the number of fluorine atoms from the highly fluorinated -$(CF_2)_7$-CF_3 alkyl chains of **1** and **2**.[22] Such an alkyl chain was anticipated to reduce potential chemical shift artifacts and reduce environmental persistence. The -S-$(CH_2)_3$-CF_2-CF_3 group found in **DD-1**–**DD-6** maintains the CF_2 group adjacent to a CH_2 which was the second most responsive fluorine group in **1** and **2**. Such a tail has been produced on large scale providing a readily available functional group as it is a key building block for the synthesis of the FDA-approved drug, Fulvestrant.[31] Finally, sulfide oxidation states were modified in **DD-2**, **DD-4**, and **DD-6** to evaluate the heteroatom effects on thermal responsiveness.

All seven new temperature sensors were synthesized under the optimized reaction conditions, enabling facile synthesis (**Figure 2**). Specifically, temperature sensors were prepared through an S_NAr reaction. Compounds **DD-2** and **DD-4** required one extra oxidation of **DD-1** and **DD-3** to provide the respective sulfones. Yields of the S_NAr reactions using thiol HS-$(CF_2)_7$-CF_3 were low, 21% to 24%, while the yields with HS-$(CH_2)_3$-CF_2-CF_3 fell in the range of 53% to 78%. In the case of **DD-2** and **DD-4**–**DD-7** the sulfur oxidation state or incorporation within the aromatic core did not lead to altered phase behavior at room temperature resulting in white solids. However, in the case of **DD-1** and **DD-3** which possess the shorter fluorinated alkyl chains and either a perfluorophenyl or perfluorobiphenyl group respectively, a room temperature liquid was obtained. These two molecules were of particular interest for facilitating future nanoparticle encapsulation studies using our established loading approach.[23]

Structure-Property Relationship Studies of Fluorinated Temperature Sensors. We next sought to investigate the temperature responsiveness of our newly synthesized compounds for comparison to both PFTBA and previously characterized compounds **1** and **2**. While our prior analyses were conducted in chloroform, here we first conducted our analyses in THF to ensure solubility of all compounds.[22] Figure 3 depicts the responsiveness for **DD-1**–**DD-7**, **1**, **2** and PFTBA under these new conditions. In this case, the thermal responsiveness is only reported for the two most responsive pairs of fluorine resonances, which in most cases remain the CF_2 group adjacent to a CH_2 group, and an aryl fluorine group. Under these conditions, all compounds led to a significant increase in responsiveness of 19% (**DD-2**) to up to 75% (**DD-3**) relative to PFTBA with a responsiveness of 9.45 × 10^{-3} ppm/°C under these conditions.

Within the data set of new fluorinated temperature sensors, the effect on responsiveness revealed a significant structure-property relationship. First, the effect of short alkyl chains with fewer ^{19}F atoms was analyzed. A comparison of matched sensor

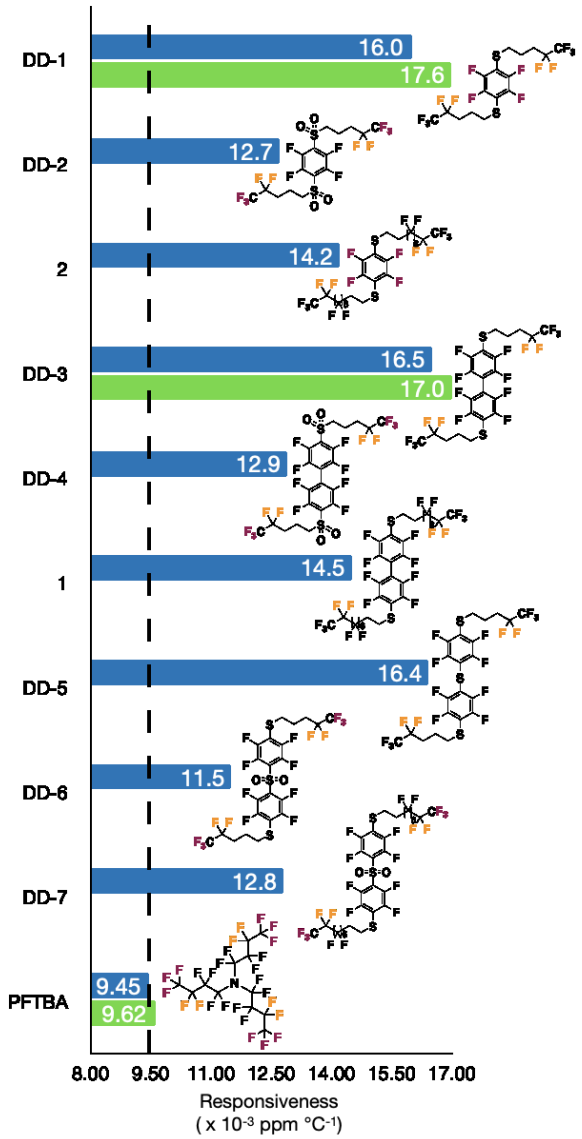

Figure 3. Responsiveness of **DD-1**–**DD-7**, compounds **1** and **2**, and PFTBA. Bars in blue are responsiveness in THF-d_8; bars in green are responsiveness in phosphate buffer. Dash line indicates thermos responsiveness of PFTBA. Fluorine groups used for temperature determination are showed in gold and maroon. Maroon coloring of the aryl fluorine group is not indicated if there is ambiguity in resonance assignment.

pairs with the same aromatic core and heteroatom oxidation state showed side chains of shorter length and fewer ^{19}F atoms to be 13% and 14% more responsive for **DD-1** versus **2**, and **DD-3** versus **1** respectively. Matched pair **DD-6** and **DD-7** containing a sulfone group was an exception where both showed a low responsiveness. The origin of this effect is explained below. Nevertheless, we conclude the short alkyl chain with fewer ^{19}F atoms remains the most beneficial when sulfones are excluded.

The effect of different aromatic cores on responsiveness was next evaluated. **DD-1**, **DD-3**, **DD-5** and **DD-6** all have the same -$(CH_2)_3$-CF_2-CF_3 fluorinated alkyl chain. In this case, **DD-1**, **DD-3** and **DD-5** have comparable responsiveness at ~16 × 10^{-3} ppm/°C, while **DD-6** containing the perfluorobiphenylsulfone core was significantly less responsive (11.5 × 10^{-3} ppm/°C) than the other three sensors. These results indicated that of the four proposed aromatic cores, no additional advantage could be determined, while sulfur oxidation of the central sulfide proved detrimental.

Surprisingly, a further look at the sulfonyl group-containing sensors revealed that the sulfonyl group whether within the core or substituted on the outer para positions of the aromatic core were also detrimental to the temperature response. In this case, **DD-2** and **DD-4**, the oxidized analogs of the highly responsive **DD-1** and **DD-3**, each lost 21% and 22% responsiveness from oxidation. The reduced responsiveness occurs based on a change in the direction of the chemical shift of the aryl fluorine in response to temperature. This resonance in **DD-2** and **DD-4** now moves upfield (**Figure S14**), whereas in **DD-1** and **DD-3** it moves downfield (**Figure 3, and S3**) providing a larger chemical shift change relative to the CF_2 resonance.

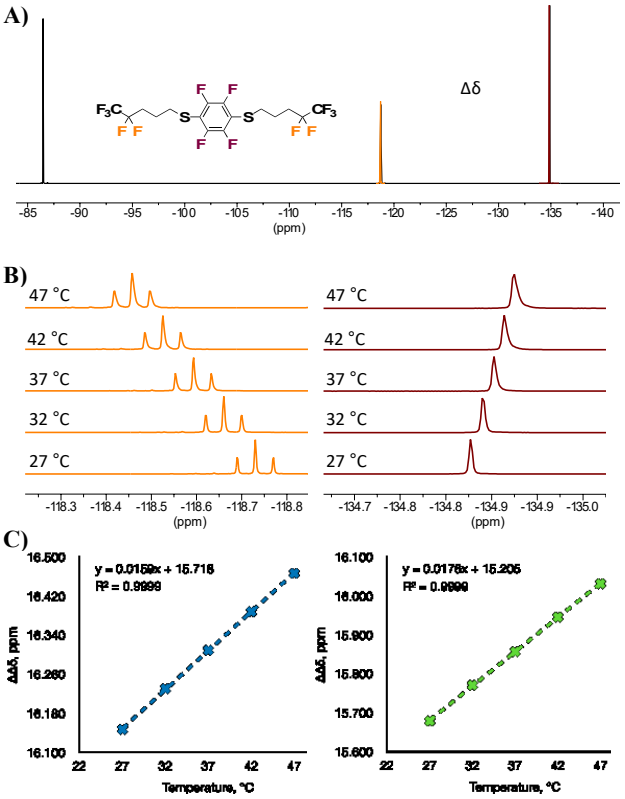

Figure 4. Spectra and temperature response of **DD-1** resonances by ^{19}F NMR. (A) Structure and spectrum of **DD-1** in THF-d_8 at 27 °C. Fluorine groups are colored to match the two resonances used to determine the temperature responsiveness. (B) Selected regions of the ^{19}F NMR spectra used for analysis with the CF_2 resonance (left) and the Ar-F (right). (C) Temperature response of **DD-1** in THF-d_8 with 16.0 ± 0.05 × 10^{-3} ppm °C^{-1} (n=3, mean ± SD) in blue and temperature response of **DD-1** in phosphate buffer with 17.6 ± 0.05 × 10^{-3} ppm °C^{-1} (n=3, mean ± SD) in green.

In addition to **DD-1** and **DD-3** having the desired liquid phase characteristics and being the most responsive sensors, these two small molecules were also shown to have sufficient aqueous solubility up to 200 µM (**Figure S13**) for analysis of their responsiveness in water, which we were unable to do with **1** and **2**. In this case, PFTBA showed an aqueous responsiveness of 9.62 x 10^{-3} ppm/°C, similar to the literature value.

DD-1 and **DD-3** showed an 83% and 77% improvement in responsiveness with 17.6 ± 0.05 × 10^{-3} ppm/°C and 17.0 ± 0.82 × 10^{-3} ppm/°C respectively.

Summarizing our initial results, of the seven new sensors, **DD-1**, **DD-3**, and **DD-5** were all more responsive than PFTBA and previously characterized **1** and **2** (**Figure 3**). In addition, **DD-1** and **DD-3** with short fluorinated alkyl tails, both form a favorable liquid phase at room temperature for future encapsulation studies with nanoparticles for ^{19}F MRI experiments (**Figure 2**), while a central sulfide in the aromatic core prevents room temperature liquid phase formation. Given their aqueous solubility, improved responsiveness could be measured for **DD-1** and **DD-3** in water, and bodes well for future biological applications with these compounds.

Degradation studies of temperature sensors, DD-1, DD-3, and DD-5 by Direct Photolysis. Our previous analysis of the environmental degradation profile of various fluorinated pharmaceuticals and model compounds revealed a significant difference in degradation propensity between fluorinated functional groups when exposed to simulated environmental photolysis or oxidative water treatment conditions.[32,33] Given concerns over the environmental persistence of highly fluorinated molecules, we evaluated the degradation profile of **DD-1**, **DD-3**, and **DD-5** under photolysis and oxidative conditions. As a first experiment, we obtained UV-Vis absorption spectra of **DD-1**, **DD-3**, and **DD-5** to evaluate the propensity to absorb sufficient light with wavelengths > 290 nm (solar light) under ambient conditions. UV-Vis spectra (**Figure S15**), show substantial overlap with the lamp output, indicating the potential for direct photolysis by sunlight or UV-lamps.

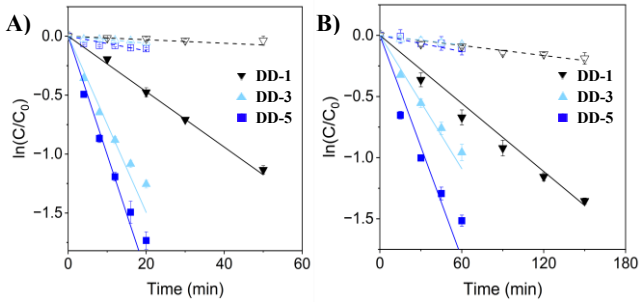

Figure 5. Photochemical degradation kinetic plots of **DD-1** (▾), **DD-3** (▲), and **DD-5** (■) at 10 µM with photolysis (filled) and dark controls (open) in (A) the mercury vapor lamp and (B) the solar simulator. (A) Under mercury vapor lamp, the kinetic rate constant of degradation of **DD-1** is 2.29 ± 0.10 × 10^{-2} min^{-1}, **DD-3** is 6.78 ± 0.71 × 10^{-2} min^{-1}, and **DD-5** is 9.29 ± 0.90 × 10^{-2} min^{-1}. (B) Under solar simulator, the kinetic rate constant of degradation of **DD-1** is 0.96 ± 0.08 × 10^{-2} min^{-1}, **DD-3** is 1.68 ± 0.17 × 10^{-2} min^{-1}, and **DD-5** is 2.80 ± 0.56 × 10^{-2} min^{-1}. Reported errors are 95% confidence intervals. Experiments were in 10 mM pH = 7 phosphate buffer and contained residual DMSO from the stock solution. Error bars indicate the standard deviation of measured concentrations of triplicate experiments.

Reverse-phase HPLC was used for quantifying degradation kinetics by direct photolysis. Under both the mercury vapor lamp and solar simulator light sources **DD-5** had the fastest rate constants followed by **DD-3** then **DD-1**, (**Figure 5**). The quantum yields, determined using the solar simulator, were 0.0272 mol Ei^{-1} for **DD-1**, 0.0267 mol Ei^{-1} for **DD-3**, and 0.0520 mol Ei^{-1} for **DD-5**, with the higher quantum yields being consistent with the fastest rate of degradation. the UV light gave higher intensity energy with more focused wavelength while solar simulator having lower intensity with more similar spectral energy distribution as of the sun.'. This is due to the high intensity UV light produced compared to the solar simulator which has a spectral energy distribution more similar to the sun. All compounds had half lives in the range of 7 to 30 minutes with the mercury vapor lamp and 25 to 72 minutes in the solar simulator.

Fluorine Mass Balance. To determine if any of the fluorinated functional groups were susceptible to degradation, we turned to quantitative ^{19}F NMR. The environmental persistence and potential impact of these fluorinated temperature sensors will be a function of not only the persistence of the parent compound, but also that of any fluorinated reaction products. Photolysis and ozonation represent natural and engineered processes, respectively, that could degrade these compounds after their use and introduction into the water system. ^{19}F NMR spectra were taken to quantify and partition degradation products from the parent compound signals for photolysis and ozonation (**Figure 6**).

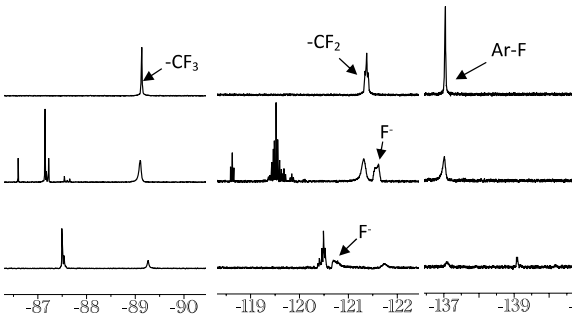

Figure 6. ^{19}F-NMR spectra of **DD-1** showing chemical shifts of fluorinated groups in the parent compound and reaction products. Top: Selected spectral regions of untreated **DD-1**. Middle: Selected spectral regions of **DD-1** following partial degradation by the solar simulator. Bottom: Selected spectral regions of **DD-1** following partial degradation by ozone. Fluoride (F^-) produced from degradation reactions is indicated for clarity. Spectra in the left, middle, and right regions are scaled differently for visibility.

Table 1 shows the mass balance for **DD-1** determined using ^{19}F NMR under photolysis and ozonation conditions. The solutions analyzed contained 50 µM of **DD-1** with 14 fluorine atoms, thus a total fluorine concentration of 700 µM, with 200 µM attributed to the aromatic fluorines (Ar-F; -137.0 ppm), 200 µM attributed to the CF_2 (-121.3 ppm), and 300 µM attributed to the CF_3 (-89.1 ppm) as shown in Figure 6. For photolysis and ozonation, 61% and 87% of the parent Ar-F signal was lost respectively. A peak at -139.1 ppm appeared following ozonation and is hypothesized to be a hydroxylated aromatic ring product, which is a known reaction process for aromatics during ozonation.[34] For the parent CF_2, the signal decreased by 45% and 79%, but new CF_2 products appeared upfield. Under both degradative conditions, new peaks appear in the near regions of the CF_2, likely due to ring opening processes. These triplets and multiplets were allocated as CF_2 because the splitting patterns and chemical shifts resemble that of CF_2 groups, and our assumption is that the CF_2 motif does not degrade. For the parent CF_3, the signal decreased by 38%

Table 1. DD-1 Mass Balance under Solar Simulator and Ozone Degradation by Quantitative ^{19}F-NMR. Parental Resonances Marked as *Italics.*

Parental Motif	δ (ppm)	Concentration (μM)	Solar Degradation Motif	δ (ppm)	Concentration (μM)	O_3 Degradation Motif	δ (ppm)	Concentration (μM)
Ar-F	*-137.0*	206	Ar-F	*-137.0*	80	Ar-F	-139.1 *-137.0*	55
$-CF_2$	*-121.3*	200	$-CF_2$	*-121.3* -118.6 to -120.6	110 98	$-CF_2$	*-121.3* -118.6 to -120.6	42 138
$-CF_3$	*-89.1*	299	$-CF_3$	*-89.1*	299[a]	$-CF_3$	*-89.1*	299[a]
			F^-	-121.5	79	F^-	-120.7	117
			Ring opening product/ Vinyl F	-86.6 to -87.5 -64.8[b]	36 3	Ring opening product/ Vinyl F	-86.6 to -87.5	48
Total fluorine: 705			Total fluorine: 705			Total fluorine: 699		

[a] $-CF_3$ is assumed to be non-degraded

[b] Corresponding regional spectrum (**Figure S18**) can be found in the Support Information.

and 69%, again with new CF_3 products appearing upfield. An excess of 39 μM and 48 μM for the solar simulator and ozonation, respectively, was found within the CF_3 region. These groups are hypothesized to be products produced by opening of the aromatic ring, which could be vinyl fluorines with oxygen and/or sulfur substituents, which could result in an upfield shift. It has previously been shown that during the photolysis or ozonation of halogenated phenols, vinyl ring opening products are possible via oxidative free radical attack.[35]

Fluoride (F^-) production via photolysis was 79 μM and 117 μM for ozonation. The F^- peak for ozonation is shifted slightly upfield compared to that of photolysis, but it was deemed the F^- peak because of the broad signal and sensitivity to solvent composition commonly seen experimentally in our previous work.[32,33] While F^- production is believed to be from the aromatic fluorines as previously demonstrated, not all the Ar-F can be accounted for via F^-.[32,33] This is supported by the sum of the concentrations of fluorine for the Ar-F, F^-, and ring opening products/vinyl fluorine being 198 μM and 200 μM for photolysis and O_3, respectively. Given ~10% error in quantification, these concentrations are equal to the initial Ar-F present. To confirm this hypothesis further mass spectrometry studies would need to be conducted. Similar trends were observed for **DD-3** and **DD-5** in the CF_2 and CF_3 region (**Figure S16**, and **S17**), with new peaks appearing near the parent CF_2 and CF_3 peaks. A difference between **DD-1** and **DD-3**/**DD-5** is that for the latter, the F^- peak is overlapping with the parent CF_2 peaks, thus F^- was calculated assuming that the CF_2 motif does not degrade.

We conclude from these degradation studies that our new temperature sensors have a sufficient UV-visible absorption cross-section to enable aromatic photolysis degradation pathways which produce F^- and ring opening products. While the aromatic cores were found to undergo chemical transformations, these studies show that the CF_2 and CF_3 motifs remain unchanged under these degradative conditions, resulting in the formation of new fluorinated degradation products. Previous studies have shown that both photolysis and H_2O_2 treatment have limited capacity to degrade CF_2 and CF_3 alkyl motifs.[36–39] Other processes using hydrated electrons,[40] photocatalysts, [39] and hydrothermal alkaline treatment [41] to degrade these moieties. Use of these treatments would require capture of excreted temperature sensors before they were introduced to the sewer system or environment.

CONCLUSION

In these studies, we have demonstrated a rational design of highly temperature responsive fluorinated small molecules for magnetic resonance-based thermometry. Two of these molecules form room temperature liquids for future encapsulation studies, and can be synthesized in a single step from readily available starting materials. These results build on our earlier results of a first-generation temperature sensor, which while more sensitive than the commonly used PFTBA, suffered from limited water solubility and was a solid at room temperature limiting facile use in aqueous systems such as through the loading into nanoparticles. Additionally, the highly fluorinated alkyl tail raised concerns over environmental persistence. In our newest designs our lead compound **DD-1** provides further improvement in temperature responsiveness, while greatly reducing the non-magnetically equivalent fluorine atoms to maintain high signal sensitivity while minimizing chemical shift artifacts. Finally, using a combined analytical approach of quantitative ^{19}F NMR and HPLC analysis, we demonstrate the advantage of using arylfluorine groups in organofluorine designs, which provide a mechanism for sufficient absorption of UV light to enhance environmental photolytic degradation and degradation under water processing conditions over more persistent aliphatic fluorine groups. Still, either further refinement of the fluorinated moieties, evaluation of additional treatment, or capture of excreted material would be needed to ensure persistent fluorinated products are not released. While not studied here, these sensors, may also find use in combination with magnetic resonance-based oximetry measurements which are temperature sensitive. Future work

will now assess this role as well as nanoparticle encapsulation for MRI-based thermometry applications.

ASSOCIATED CONTENT

Supporting Information

Description of synthesis of **DD-1–DD-7**; ^{1}H, ^{13}C, and ^{19}F NMR characterization of **DD-1–DD-7**; description of temperature responsiveness determination; description of HPLC method for degradation monitoring; description of UV spectra experiment and quantum yield determination; description of ^{19}F NMR for mass balance; temperature measurement and responsiveness determination of **DD-1–DD-7**, compound **1** and **2**, PFTBA; solubility determination of **DD-1**; temperature response of aryl ^{19}F resonances on temperature sensors; spectra of degradation irradiation and compounds' UV absorption; ^{19}F NMR degradation spectra of **DD-1**, **DD-3**, and **DD-5**; and mass balance under solar simulator by quantitative ^{19}F NMR of **DD-3** and **DD-5**.

AUTHOR INFORMATION

Corresponding Author

William C.K. Pomerantz − *University of Minnesota*, Minneapolis, Minnesota 55414, United States; orcid.org/ 0000-0002-0163-4078; Email: wcp@umn.edu

Author Contributions

J.Q. performed the organic synthesis and temperature dependent ^{19}F NMR experiments. T.M. performed the degradation studies. T.G.S performed the $\{^{1}H+^{19}F\}$ decoupling ^{13}C NMR studies. W.A.A helped design the degradation experiments and analysis of the data. W.C.K.P oversaw all experimental design and interpretation of experimental data. The manuscript was written through contributions of all authors. All authors have given approval to the final version of the manuscript.

ACKNOWLEDGMENT

Funding for this project was provided by the Minnesota Environment and Natural Resources Trust Fund as recommended by the Legislative-Citizen Commission on Minnesota Resources (LCCMR) and NIH MIRA award R35GM140837-02 (W.C.K.P)

REFERENCES

(1) Rieke, V.; Butts Pauly, K. MR Thermometry. *Journal of Magnetic Resonance Imaging* **2008**, *27* (2), 376–390.

(2) Kim, J. H.; Hahn, E. W. Clinical and Biological Studies of Localized Hyperthermia. *Cancer Res* **1979**, *39* (6_Part_2), 2258–2261.

(3) Polderman, K. H.; Herold, I. Therapeutic Hypothermia and Controlled Normothermia in the Intensive Care Unit: Practical Considerations, Side Effects, and Cooling Methods*. *Crit Care Med* **2009**, *37* (3).

(4) DINERMAN, J. A. Y. L.; BERGER, R. D.; CALKINS, H. Temperature Monitoring During Radiofrequency Ablation. *J Cardiovasc Electrophysiol* **1996**, *7* (2), 163–173.

(5) Zhu, M.; Sun, Z.; Ng, C. K. Image-Guided Thermal Ablation with MR-Based Thermometry. *Quant Imaging Med Surg* **2017**, *7* (3), 356.

(6) Chapelin, F.; Gedaly, R.; Sweeney, Z.; Gossett, L. J. Prognostic Value of Fluorine-19 MRI Oximetry Monitoring in Cancer. *Mol Imaging Biol* **2021**, 1–12.

(7) Hindman, J. C. Proton Resonance Shift of Water in the Gas and Liquid States. *J Chem Phys* **1966**, *44* (12), 4582–4592.

(8) Silletta, E. v; Jerschow, A.; Madelin, G.; Alon, L. Multinuclear Absolute Magnetic Resonance Thermometry. *Commun Phys* **2019**, *2* (1), 1–10.

(9) Schilling, F.; Schröder, L.; Palaniappan, K. K.; Zapf, S.; Wemmer, D. E.; Pines, A. MRI Thermometry Based on Encapsulated Hyperpolarized Xenon. *ChemPhysChem* **2010**, *11* (16), 3529–3533.

(10) Janjic, J. M.; Ahrens, E. T. Fluorine-Containing Nanoemulsions for MRI Cell Tracking. *WIREs Nanomedicine and Nanobiotechnology* **2009**, *1* (5), 492–501.

(11) Thorarinsdottir, A. E.; Gaudette, A. I.; Harris, T. D. Spin-Crossover and High-Spin Iron (II) Complexes as Chemical Shift 19 F Magnetic Resonance Thermometers. *Chem Sci* **2017**, *8* (3), 2448–2456.

(12) Prinz, C.; Delgado, P. R.; Eigentler, T. W.; Starke, L.; Niendorf, T.; Waiczies, S. Toward 19F Magnetic Resonance Thermometry: Spin–Lattice and Spin–Spin-Relaxation Times and Temperature Dependence of Fluorinated Drugs at 9.4 T. *Magnetic Resonance Materials in Physics, Biology and Medicine* **2019**, *32* (1), 51–61.

(13) Krafft, M. P.; Riess, J. G. Therapeutic Oxygen Delivery by Perfluorocarbon-Based Colloids. *Adv Colloid Interface Sci* **2021**, *294*, 102407.

(14) Miller, M. A.; Sletten, E. M. Perfluorocarbons in Chemical Biology. *ChemBioChem* **2020**, *21* (24), 3451–3462.

(15) Kadakia, R. T.; Xie, D.; Guo, H.; Bouley, B.; Yu, M.; Que, E. L. Responsive Fluorinated Nanoemulsions for 19F Magnetic Resonance Detection of Cellular Hypoxia. *Dalton Transactions* **2020**, *49* (45), 16419–16424.

(16) Berkowitz, B. A.; Handa, J. T.; Wilson, C. A. Perfluorocarbon Temperature Measurements Using 19F NMR. *NMR Biomed* **1992**, *5* (2), 65–68.

(17) Mason, R. P. Non-Invasive Physiology: 19F NMR of Perfluorocarbons. *Artificial Cells, Blood Substitutes, and Biotechnology* **1994**, *22* (4), 1141–1153.

(18) Staal, A. H. J.; Veltien, A.; Srinivas, M.; Scheenen, T. W. J. 19F MRI Imaging Strategies to Reduce

Isoflurane Artifacts in In Vivo Images. *Mol Imaging Biol* **2022**, *24* (1), 71–81.

(19) Hong, A. C.; Young, C. J.; Hurley, M. D.; Wallington, T. J.; Mabury, S. A. Perfluorotributylamine: A Novel Long-lived Greenhouse Gas. *Geophys Res Lett* **2013**, *40* (22), 6010–6015.

(20) Cousins, I. T.; DeWitt, J. C.; Glüge, J.; Goldenman, G.; Herzke, D.; Lohmann, R.; Ng, C. A.; Scheringer, M.; Wang, Z. The High Persistence of PFAS Is Sufficient for Their Management as a Chemical Class. *Environ Sci Process Impacts* **2020**, *22* (12), 2307–2312.

(21) Guelfo, J. L.; Korzeniowski, S.; Mills, M. A.; Anderson, J.; Anderson, R. H.; Arblaster, J. A.; Conder, J. M.; Cousins, I. T.; Dasu, K.; Henry, B. J.; Lee, L. S.; Liu, J.; McKenzie, E. R.; Willey, J. Environmental Sources, Chemistry, Fate, and Transport of Per- and Polyfluoroalkyl Substances: State of the Science, Key Knowledge Gaps, and Recommendations Presented at the August 2019 SETAC Focus Topic Meeting. *Environ Toxicol Chem* **2021**, *40* (12), 3234–3260.

(22) Lee, A. L.; Pandey, A. K.; Chiniforoush, S.; Mandal, M.; Li, J.; Cramer, C. J.; Haynes, C. L.; Pomerantz, W. C. K. Development of a Highly Responsive Organofluorine Temperature Sensor for 19F Magnetic Resonance Applications. *Anal Chem* **2022**, *94* (9), 3782–3790.

(23) Lee, A. L.; Lee, S.-H.; Nguyen, H.; Cahill, M.; Kappel, E.; Pomerantz, W. C. K.; Haynes, C. L. Investigation of the Post-Synthetic Confinement of Fluorous Liquids Inside Mesoporous Silica Nanoparticles. *Langmuir* **2021**, *37* (17), 5222–5231.

(24) Trang, B.; Li, Y.; Xue, X.-S.; Ateia, M.; Houk, K. N.; Dichtel, W. R. Low-Temperature Mineralization of Perfluorocarboxylic Acids. *Science (1979)* **2022**, *377* (6608), 839–845.

(25) Dulin, David.; Mill, Theodore. Development and Evaluation of Sunlight Actinometers. *Environ Sci Technol* **1982**, *16* (11), 815–820.

(26) Leifer, A. *The Kinetics of Environmental Aquatic Photochemistry: Theory and Practice*; American Chemical Society, 1988.

(27) Laszakovits, J. R.; Berg, S. M.; Anderson, B. G.; O'Brien, J. E.; Wammer, K. H.; Sharpless, C. M. P-Nitroanisole/Pyridine and p-Nitroacetophenone/Pyridine Actinometers Revisited: Quantum Yield in Comparison to Ferrioxalate. *Environ Sci Technol Lett* **2017**, *4* (1), 11–14.

(28) Bader, H.; Hoigné, J. Determination of Ozone in Water by the Indigo Method. *Water Res* **1981**, *15* (4), 449–456.

(29) von Sonntag, C.; von Gunten, U. *Chemistry of Ozone in Water and Wastewater Treatment*; IWA publishing, 2012.

(30) Bourgin, M.; Beck, B.; Boehler, M.; Borowska, E.; Fleiner, J.; Salhi, E.; Teichler, R.; von Gunten, U.; Siegrist, H.; McArdell, C. S. Evaluation of a Full-Scale Wastewater Treatment Plant Upgraded with Ozonation and Biological Post-Treatments: Abatement of Micropollutants, Formation of Transformation Products and Oxidation by-Products. *Water Res* **2018**, *129*, 486–498.

(31) Pichandi Mohanraj, S. K.; Tulasi, R.; Chidambaram Subramanian, V. An Efficient Regioselective Preparation of Fulvestrant. *Org Prep Proced Int* **2021**, *53* (4), 362–368.

(32) Bhat, A. P.; Pomerantz, W. C. K.; Arnold, W. A. Finding Fluorine: Photoproduct Formation during the Photolysis of Fluorinated Pesticides. *Environ Sci Technol* **2022**, *56* (17), 12336–12346.

(33) Bhat, A. P.; Mundhenke, T. F.; Whiting, Q. T.; Peterson, A. A.; Pomerantz, W. C. K.; Arnold, W. A. Tracking Fluorine during Aqueous Photolysis and Advanced UV Treatment of Fluorinated Phenols and Pharmaceuticals Using a Combined 19F-NMR, Chromatography, and Mass Spectrometry Approach. *ACS Environmental Au* **2022**, *2* (3), 242–252.

(34) Tay, K. S.; Rahman, N. A.; Abas, M.; Bin, R. Ozonation of Metoprolol in Aqueous Solution: Ozonation by-Products and Mechanisms of Degradation. *Environmental Science and Pollution Research* **2013**, *20* (5), 3115–3121.

(35) Vialaton, D.; Richard, C.; Baglio, D.; Paya-Perez, A.-B. Phototransformation of 4-Chloro-2-Methylphenol in Water: Influence of Humic Substances on the Reaction. *J Photochem Photobiol A Chem* **1998**, *119* (1), 39–45.

(36) Taniyasu, S.; Yamashita, N.; Yamazaki, E.; Petrick, G.; Kannan, K. The Environmental Photolysis of Perfluorooctanesulfonate, Perfluorooctanoate, and Related Fluorochemicals. *Chemosphere* **2013**, *90* (5), 1686–1692.

(37) Houtz, E. F.; Sedlak, D. L. Oxidative Conversion as a Means of Detecting Precursors to Perfluoroalkyl Acids in Urban Runoff. *Environ Sci Technol* **2012**, *46* (17), 9342–9349.

(38) Hori, H.; Hayakawa, E.; Einaga, H.; Kutsuna, S.; Koike, K.; Ibusuki, T.; Kiatagawa, H.; Arakawa, R. Decomposition of Environmentally Persistent Perfluorooctanoic Acid in Water by Photochemical Approaches. *Environ Sci Technol* **2004**, *38* (22), 6118–6124.

(39) Liu, F.; Guan, X.; Xiao, F. Photodegradation of Per- and Polyfluoroalkyl Substances in Water: A Review

of Fundamentals and Applications. *J Hazard Mater* **2022**, *439*, 129580.

(40) Bentel, M. J.; Yu, Y.; Xu, L.; Li, Z.; Wong, B. M.; Men, Y.; Liu, J. Defluorination of Per-and Polyfluoroalkyl Substances (PFASs) with Hydrated Electrons: Structural Dependence and Implications to PFAS Remediation and Management. *Environ Sci Technol* **2019**, *53* (7), 3718–3728.

(41) Hao, S.; Choi, Y.-J.; Wu, B.; Higgins, C. P.; Deeb, R.; Strathmann, T. J. Hydrothermal Alkaline Treatment for Destruction of Per-and Polyfluoroalkyl Substances in Aqueous Film-Forming Foam. *Environ Sci Technol* **2021**, *55* (5), 3283–3295.

(Word Style "TF_References_Section"). References are placed at the end of the manuscript. Authors are responsible for the accuracy and completeness of all references. Examples of the recommended formats for the various reference types can be found at http://pubs.acs.org/page/4authors/index.html. Detailed information on reference style can be found in The ACS Style Guide, available from Oxford Press.

To format double-column figures, schemes, charts, and tables, use the following instructions:

Place the insertion point where you want to change the number of columns
From the **Insert** menu, choose **Break**
Under **Sections**, choose **Continuous**
Make sure the insertion point is in the new section. From the **Format** menu, choose **Columns**
In the **Number of Columns** box, type **1**
Choose the **OK** button

Now your page is set up so that figures, schemes, charts, and tables can span two columns. These must appear at the top of the page. Be sure to add another section break after the table and change it back to two columns with a spacing of 0.33 in.

Insert Table of Contents artwork here